Chapter 5

Hyperpolarized Gas Imaging on a Low-Field Pulsed Resistive System

5.1 Background

MR imaging with hyperpolarized helium and xenon is an alternative to conventional proton MR imaging, especially for imaging void spaces, such as lungs [16, 39, 9] and colon [87], which contain no water. Initially, most of the hyperpolarized gas imaging was done on commercially available middle and high field scanners [16, 40, 43, 11, 88], mainly because of the availability to the MRI community. However, in Chapter 3.2.3 we show that the SNR of hyperpolarized gas is independent of the imaging field strength once the body becomes the dominant source of noise (so-called "body-noise dominance") [22, 23, 21, 20]. Since the transition from coil-noise to body-noise dominance occurs at about 1 MHz (23.5 mT) for human torsos and 4 MHz (94 mT) for heads [20], hyperpolarized gas MR can be performed at low-field with no loss in the SNR of the image.

Low-field imaging offers important advantages over the high-field imaging. The low-field MR system is straightforward and inexpensive to build, since a homogeneous magnetic field can be produced with a homogeneous wire-wound electromagnets and the low Larmor frequencies reduce RF power requirements and allow the use of commonly available electronic components. The low-field systems are easy to site as they do not require specialized accommodations, such as a shielded room or cryogenic cooling of the magnet [21]. One of the biggest advantages of low-field MRI is the reduced susceptibility differences in heterogeneous samples and reduced static field inhomogeneities at low-field, which can cause significant distortions and signal loss at high-field strengths.

Low-field imaging of hyperpolarized gas has been performed mainly with static elec-

tromagnets [21, 47, 71, 72, 89, 26, 90]. Some attempts have also been made to image hyperpolarized gases with SQUIDS [91]. However, there are several advantages in using a pulsed, rather than a static resistive system. A pulsed magnet is lighter than the permanent magnet and it can be designed to produce practically no eddy currents which can distort the image. Another important advantage is that the pulsed electromagnet allows for the adjustment of the current strength and so eliminates the need to retune the RF coils for imaging different species (^{129}Xe, ^{3}He, water, fluoride). Because of the low duty-cycle, pulse mode power supplies are ideally suited to the brief imaging window of hyperpolarized gas MRI, especially when used in conjunction with single-shot techniques, such as RARE and trueFISP. Finally, a pulsed MR scanner is compatible with prepolarized proton MRI [25, 24] (see Chapter 3), and would therefore enable hyperpolarized gas as well as proton MRI on a single low-field scanner [92].

In addition to the many advantages offered by the pulsed resistive low-field MRI scanner, the system also presents several challenges. As discussed in Chapter 3, the readout field must be temporally and spatially stable to better than 100 ppm. There are several possible sources of field instability. First, the magnetic field could vary as a result of power supply instability. This problem was solved by using high-precision electronic components. Second, the strength of the magnetic field at the position of the sample changes due to the resistive heating of the copper wires which expand slightly outward from the center of the magnet bore. ^{129}Xe and ^{3}He T_2^{CPMG} measurements described in Section 4.6 produced spin echo trains containing 4096 echoes and lasting tens of seconds which demonstrated that the resistive heating of the magnet coils had negligible effect on the temporal stability of the magnetic field at low magnetic field strengths (frequency of 397 kHz). Another challenge was to investigate the effect of field-switching on the hyperpolarization of the noble gas, especially since there has been minimal research done in this area. We anticipated that the field-switching might destroy some or all of the gas hyperpolarization due to nonadiabatic changes in the alignment of the gas magnetization, between the direction parallel to the readout field and the direction parallel to the Earth's field. The experiments described in Chapter 4.5.2 confirmed the need for hardware and software adjustments to the pulsed resistive MRI scanner.

The experiments presented in the previous chapter established the possibility of using a pulsed low-field resistive system for hyperpolarized gas imaging. They also helped us to

determine two important parameters–the diffusion coefficient and the T_2 relaxation time of hyperpolarized ^{129}Xe and ^{3}He–both of which make hyperpolarized gas imaging very different from proton imaging. In this chapter we will examine how these parameters affect the design of pulse-sequences used in imaging hyperpolarized gases. In particular, we will try to focus on two issues: 1. How to make best use of the nonrenewable hyperpolarization of the noble gas; 2. How to minimize the large diffusion of hyperpolarized gases. To answer these questions we will develop a model of signal decay during gradient echo and spin echo imaging. We will show that the hyperpolarized gas signal is best utilized using a CPMG spin echo sequence (also called RARE) while diffusion is minimized by first collecting the low k-values using centrally ordered phase-encode gradients. Consequently, the sequence that satisfies both requirements is a RARE sequence with centrally ordered phase-encode gradients.

5.2 Basic Principles of MR Imaging

In Section 3.2.1 we derived the MR signal equation (see Eqs. 3.1 and 3.5). We would now like to build upon this equation to show how imaging of the nuclear spin density can be performed using imaging gradients.

Ignoring the strength of the field generated by the transmit coil (B_1) and the flux though the receiver coil ($\propto i\omega_\circ$), the MR signal is the sum of magnetic moments throughout the imaging volume,

$$s(t) = \int_V M(x, y, z)\, dV. \tag{5.1}$$

The magnetic moments have magnitude, $M_\circ$, and phase, ϕ, so that

$$s(t) = \int_x \int_y \int_z M_\circ(x, y, z) e^{-i\phi(x,y,z,t)}\, dx\, dy\, dz. \tag{5.2}$$

If imaging is slice-selective, we can immediately integrate over the z-coordinate and define the magnetization in a slice of thickness Δz, centered around $z_\circ$, as

$$m(x, y) \equiv \int_{z_\circ - \delta z/2}^{z_\circ + \delta z/2} M_\circ(x, y, z) e^{-i\phi(x,y,z,t)}\, dz. \tag{5.3}$$

The phase of the magnetic moment can be expressed from the Larmor relationship as

$$\phi(t) = \gamma \int_0^t B(x, y, \tau)\, d\tau, \tag{5.4}$$

where the magnetic field is a sum of the static magnetic field and the imaging gradients, $B(x, y, \tau) = B_\circ + \mathbf{G} \cdot \mathbf{r}$; while the magnetization magnitude decays due to T_2 relaxation, $m(x, y) = m_\circ(x, y) \exp(-t/T_2)$. Therefore,

$$s(t) = \int_x \int_y m_\circ(x, y) e^{(-t/T_2)} e^{-i\omega_\circ t} e^{-i\gamma \int_0^t (\mathbf{G}(\tau)\cdot\mathbf{r}) d\tau}\, dx\, dy. \tag{5.5}$$

To simplify the present analysis, we will ignore the T_2 relaxation for the moment. Furthermore, the $\exp(-i\omega_\circ t)$ term can be dropped since the detection apparatus demodulates the carrier frequency by multiplying the received signal by $\exp(+i\omega_\circ t)$. The remaining term

contains the imaging gradients which are central to our discussion:

$$s(t) = \int_x \int_y m_\circ(x,y) exp\Big\{-i\gamma \int_0^t \left[G_x(\tau)x + G_y(\tau)y\right]\, d\tau\Big\}\, dx\, dy. \tag{5.6}$$

Equation 5.6 tells us that the imaging gradients control the phase of the precessing magnetization. We can express the gradients in terms of the spatial frequency vector, **k**:

$$\begin{aligned} k_x &\equiv \frac{\gamma}{2\pi}\int_0^t G_x(\tau)\, d\tau \\ k_y &\equiv \frac{\gamma}{2\pi}\int_0^t G_y(\tau)\, d\tau. \end{aligned} \tag{5.7}$$

The MR signal is thus

$$s(t) = \int_x \int_y m_\circ(x,y) e^{-i2\pi[k_x(t)x + k_y(t)y]}\, dx\, dy, \tag{5.8}$$

where $s(t)$ can be viewed as the sampling of trajectories of $k_x(t)$ and $k_y(t)$. From this last representation of the MR signal equation, we can clearly see that the detected MR signal is the two dimensional Fourier transform (2DFT) of the spin density distribution:

$$s(t) = F_{2D}\{m(x,y)\}. \tag{5.9}$$

This is an important result of MRI physics. It means that the imaging problem is reduced to acquiring the signal $s(t)$ at a range of values (k_x, k_y) and then inverting Eq. 5.8 using the inverse Fourier transform function (2DFT^{-1}).

There are many possible ways of sampling the k-space, each with its own advantages and uses, but the one that is most readily applicable to 2DFT is the Cartesian sampling of k-space, shown in Figure 5.1. Equation 5.7 tells us that the different k-values can be accessed by either changing the size of the imaging gradient or by changing the upper limit of the time integral. The former method is used for phase-encoding along the y-direction (also called the phase-encode direction), while the later method is used for encoding along the x-direction (also called the readout direction). Consequently,

$$\Delta k_x = \frac{\gamma}{2\pi}\, G_x\, \Delta t \tag{5.10}$$

$$\Delta k_y = \frac{\gamma}{2\pi}\, \Delta G_y\, t_{Gy}. \tag{5.11}$$

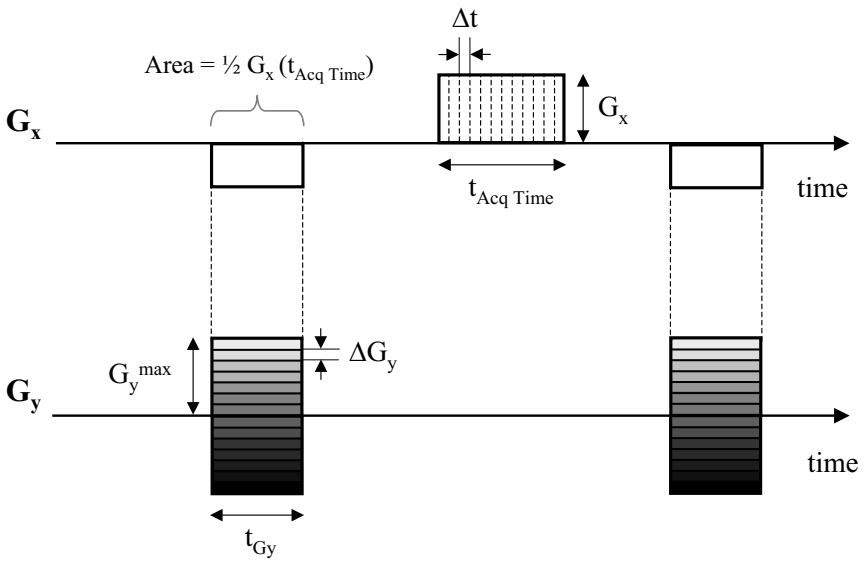

Figure 5.1: A typical gradient waveform used for collecting k-space data. Data acquisition occurs during the application of the positive G_x lobe. The magnitude of G_y is decremented with each excitation, while the magnitude of G_x is kept constant.

The k-space trajectory is described in Figure 5.2. The x and y-gradients turn on simultaneously for a time Δt_{Gy}, and the k-space trajectory moves to the point

$$k_{x,1} = -\frac{\gamma}{2\pi}\,\frac{1}{2}G_x\; t_{Acq.\,Time},\;\; k_{y,1} = \frac{\gamma}{2\pi}\,G_y^{max}\; t_{Gy}.$$

Once the y-gradient is turned off, the signal is read out in the presence of a constant x-gradient of amplitude G_x and duration $t_{Acq\,Time}$. The k-space trajectory moves along a constant k_y axis to the point

$$k_{x,2} = -k_{x,1},\;\; k_{y,2} = k_{y,1}.$$

On subsequent excitations, the amplitude of the y-gradient lobe is decremented (or incremented) while the x-gradient remains the same. This way, a new line of k-space is sampled after each excitation. Eventually, a sufficient amount of 2-D transform space is sampled to perform an inverse 2-D Fourier transform in order to reconstruct the object space, $m(x, y)$.

The study of pulse-sequence design examines ways in which k-space could be traversed

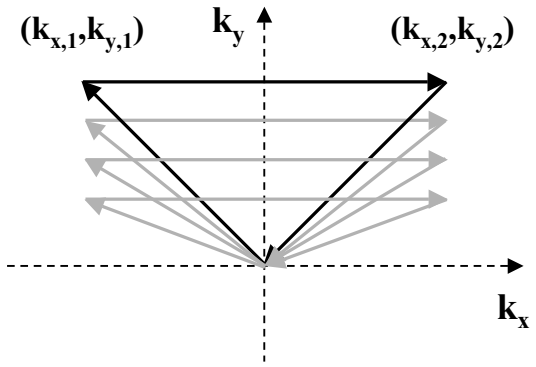

Figure 5.2: A schematic representation of k-space data collection. A line of k-space is acquired during each data acquisition; multiple acquisitions with varying k_y values are required to scan the entire plane.

so as to minimize imaging artifacts while maximizing the SNR and resolution of the image. In this work we will focus on two standard imaging sequences–the gradient echo and spin echo sequence.

5.3 Theoretical Model of Signal Decay during Hyperpolarized Gas Imaging

The estimation of T_2 relaxation and diffusion coefficients of hyperpolarized gases presented in Chapter 4 enables us to model the amount of signal decay during an imaging sequence. We can divide the effects which decrease the size of hyperpolarized gas signal into three groups: the effect of the excitation flip-angle; T_1 and T_2 relaxation losses; and diffusion-induced losses. We now examine each one of these effects in more detail.

5.3.1 Flip-Angle Effect

Since the signal detected in the receiver coil is due to the precession of the *transverse* magnetization, we need to estimate the projection of the longitudinal magnetization vector onto the transverse axis after each excitation. If a flip-angle α is used for each excitation, then the longitudinal components before and the transverse components after the first, second, and the nth excitations (where $n = 1, 2, ..., N$) are, respectively (see Figure 5.3),

$$\begin{aligned} m_{z,0} &= m_\circ, & m_{xy,1} &= m_\circ(\sin\alpha), \\ m_{z,1} &= m_\circ(\cos\alpha), & m_{xy,2} &= m_\circ(\cos\alpha)(\sin\alpha), \\ m_{z,n-1} &= m_\circ(\cos^{n-1}\alpha), & m_{xy,n} &= m_\circ(\cos^{n-1}\alpha)(\sin\alpha). \end{aligned} \tag{5.12}$$

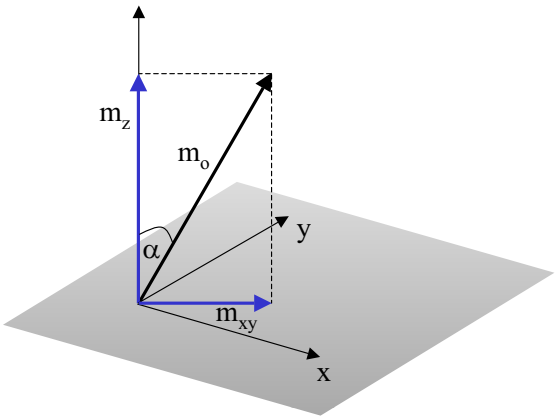

Figure 5.3: Projection of magnetization onto the longitudinal and transverse axis.

If a 90-degree flip-angle is used, then $m_{xy,1} = m_\circ$ and $m_{xy,2} = m_{xy,n} = 0$. In other words, because of the nonrenewable nature of the gas polarization, there can be no further excitations after the entire gas magnetization has been tipped into the transverse plane. In contrast, proton imaging allows the use of multiple 90-degree excitations, provided the time between the excitations is sufficiently long for the build-up of the longitudinal thermal proton magnetization.

The transverse magnetization after the nth excitation replaces the $m_\circ(x, y)$ term in Eq. 5.8, so that the NMR signal is

$$\begin{aligned} s(t) &= \int_x \int_y m_\circ \, \cos^{n-1}\alpha \, \sin\alpha \; e^{-i2\pi[k_x(t)x + k_y(t)y]} \, dx \, dy \\ &= \cos^{n-1}\alpha \, \sin\alpha \int_x \int_y m_\circ \, e^{-i2\pi[k_x(t)x + k_y(t)y]} \, dx \, dy \\ &= s_\circ(t) \, \left\{ \cos^{n-1}\alpha \, \sin\alpha \right\}, \end{aligned} \tag{5.13}$$

where $s_\circ(t)$ is

$$s_\circ(t) = \int_x \int_y m_\circ \, e^{-i2\pi[k_x(t)x + k_y(t)y]} \, dx \, dy, \tag{5.14}$$

while the term in the brackets is the weighting (scaling) function representing the effect of the RF flip-angle. The expression above assumes that the flip-angle α is homogeneous across the sample (i.e., is independent of x and y-coordinates) so that the cosine and sine terms can be pulled out of the integral. This assumption is correct only if the sample is smaller than the region of homogeneity of the RF coils. If this is not the case, the above expression is at best an approximation. The weighting function can be manipulated by variable flip-angles to achieve equal weighting of k-space lines [93].

5.3.2 Signal Decay due to T_1 and T_2 Relaxation

Signal loss is also caused by the relaxation mechanisms. According to Bloch equations [59], the transverse signal decays with a time constant T_2, while the longitudinal signal of the hyperpolarized gas decays with the time constant T_1 towards its thermal equilibrium.[1] Equation 5.12 tells us that in the absence of any relaxation, the transverse magnetization

[1]The T_1 relaxation represents the relaxation of the longitudinal magnetization component towards the thermal polarization levels along the z-axis. Therefore, in the case of *hyperpolarized* gases with polarization levels well above the thermal equilibrium, the T_1 relaxation represents the *decay* of hyperpolarization, while for *water*, T_1 relaxation represents the *growth* of magnetization along the longitudinal axis.

after the nth excitation, $m_{xy,n}$, can be expressed in terms of the longitudinal component before the nth excitation, $m_{z,n-1}$, as $m_{xy,n} = m_{z,n-1} \sin\alpha$. Scaling the transverse magnetization by the transverse relaxation, $\exp(-t/T_2)$, and the longitudinal magnetization by the longitudinal relaxation, $\exp(-t/T_1)$, we get

$$\begin{aligned} m_{xy,n} \exp(-\frac{t_2}{T_2}) &= m_{z,n-1}\ \sin\alpha\ \exp(-\frac{t_1}{T_1}) \exp(-\frac{t_2}{T_2}) \\ &= m_\circ\ \cos^{n-1}\alpha\ \sin\alpha\ \exp(-\frac{t_1}{T_1}) \exp(-\frac{t_2}{T_2}), \end{aligned} \tag{5.15}$$

where t_1 is the time elapsed from the first to the nth RF excitation and could be on the order of seconds, while t_2 is the time since the nth RF excitation and is usually on the order of milliseconds.

The NMR signal can again be obtained from Eq. 5.8, by replacing the $m_\circ$ term with the final expression in Eq. 5.15, so that

$$\begin{aligned} s(t) &= \int_x \int_y m_\circ\ \cos^{n-1}\alpha\ \sin\alpha\ e^{-t_1/T_1}\ e^{-t_2/T_2}\ e^{-i2\pi[k_x(t)x + k_y(t)y]}\ dx\ dy \\ &= s_\circ(t) \left\{\cos^{n-1}\alpha\ \sin\alpha\right\} \left\{e^{-t_1/T_1}\ e^{-t_2/T_2}\right\}, \end{aligned} \tag{5.16}$$

where we again assumed that the flip-angle and the relaxation rates do not change across the sample. Comparing Eq. 5.16 with Eq. 5.13 we can conclude that the exponential term in Eq. 5.16 is the contribution of T_1 and T_2 relaxation to signal loss.

When using the CPMG spin echo imaging sequence, we will only be concerned with the transverse relaxation time constant since the magnetization is constantly in the transverse axis during imaging. In particular, the T_2 relaxation should be replaced with the T_2^{CPMG} relaxation time, because the imaging sequences were acquired in the presence of background gradients (see Section 4.3 for more details). On the other hand, when using the gradient echo imaging sequence, T_2 relaxation time should be replaced with T_2^* time constant to include signal decay due to gradient inhomogeneities. In addition, when imaging ^{3}He, T_1 decay can be ignored, since the T_1 relaxation times of ^{3}He are on the order of hours, while the imaging time is on the order of seconds.

5.3.3 Signal Decay due to Diffusion

In Section 4.4.1 (Eqs. 4.41 and 4.42) we derived an expression for signal decay due to diffusion in an arbitrary gradient form $\mathbf{g}(\tau)$,

$$\exp\left[-D\gamma^2\int_0^t\left(\int_0^{t'}\mathbf{g}(\tau)d\tau\right)^2dt'\right]=\exp\left[-4\pi^2D\int_0^t\left(k_x^2(t')+k_y^2(t')\right)dt'\right], \tag{5.17}$$

where D is the diffusion coefficient. Since the gradient waveform is known from the pulse sequence used in the imaging experiments and the diffusion coefficients of hyperpolarized ^{129}Xe and ^{3}He have been estimated in Section 4.7, we can use Eq. 5.17 to model diffusion losses as a function of imaging time.

The NMR signal in the presence of diffusion losses is

$$\begin{aligned} s(t) &= \int_x\int_y m_\circ\, e^{-4\pi^2D\int_0^t\left[k_x^2(t')+k_y^2(t')\right]dt'}\, e^{-i2\pi[k_x(t)x+k_y(t)y]}\,dx\,dy \\ &= s_\circ(t)\left\{e^{-4\pi^2D\int_0^t\left[k_x^2(t')+k_y^2(t')\right]dt'}\right\}, \end{aligned} \tag{5.18}$$

where again we were able to pull the diffusion term out of the integral because the gradient waveform is assumed to be uniform across the sample (i.e., G_x and G_y have no spatial dependence).

5.3.4 K-Space Weighting

Knowing the various processes that contribute to MR signal decay we are now able to construct so-called *"k*-space weighting" which modulates (weights or scales) the MR time-domain data.

In all the imaging experiments, the object imaged was a sphere, 2.5 cm in diameter, filled with either hyperpolarized ^{129}Xe, ^{3}He or water. Since no gradients were applied along the z-axis, the imaging was slice non-selective. This meant that we were imaging the projection of a sphere onto a plane orthogonal to the z-axis, which was a circle of varying signal intensity. The intensity is greatest at the center of the circle, since it corresponds to the projection through the center of the sphere, and falls off to zero at the sphere's borders.

Because data acquisition happens in time (or k-space) domain, we have to consider the Fourier transform of a circle–which is a jinc function (see Figure 5.5). However, since k-

space signal is subjected to the decay processes described in the previous section, the jinc function has to be scaled by a function describing the amount of signal decay along the readout (x) and phase-encode (y) directions. We call such a scaling function the "k-space weighting". The k-space weighting can easily be constructed once we are able to evaluate all the scaling terms from Eqs. 5.13, 5.16, and 5.18 pertaining to a particular pulse sequence. For a general case, the k-space weighting w is

$$w(t) = \left\{\cos^{n-1}\alpha \sin\alpha\right\} \left\{e^{-t_1/T_1} e^{-t_2/T_2}\right\} \left\{e^{-4\pi^2 D \int_0^t \left[k_x^2(t') + k_y^2(t')\right] dt'}\right\}. \tag{5.19}$$

The product of the jinc and w functions is then transformed into the image domain using 2-D inverse Fourier transform. The result, when displayed in the image mode as in Figure 5.5, is a circle that has been convolved with the inverse Fourier transform of the k-space weighting function.[2] The entire procedure is schematically illustrated in Figures 5.5 and 5.4.

The procedure described above served as a the basis for a Matlab simulation which modelled signal decay given specific pulse-sequence parameters (see Appendix C) and resulted in a weighted (scaled) projection of a sphere in both, k-space and object-space domains.

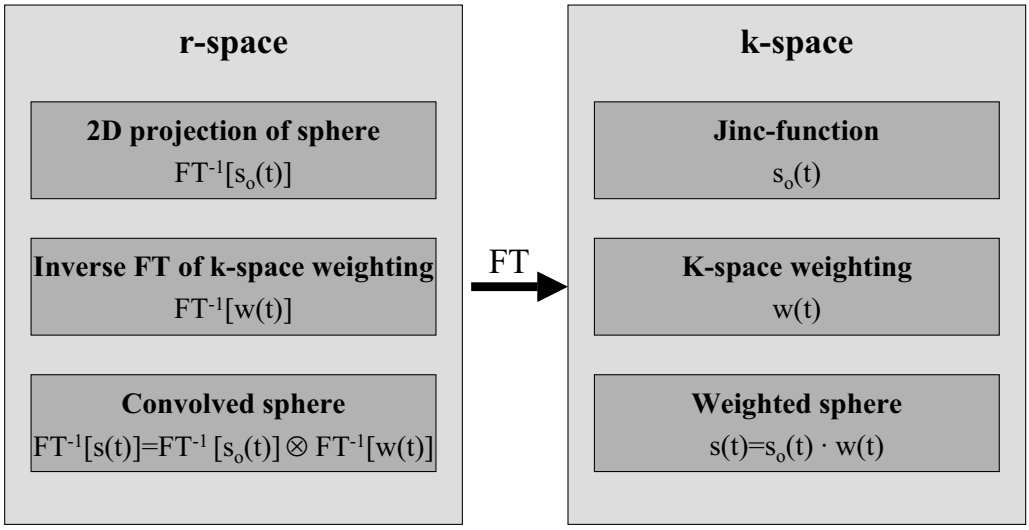

Figure 5.4: Overview of r-space and k-space functions used in modelling the effects of signal decay on the image of a 2-D sphere.

[2] According to the theorem of Fourier transforms [94], multiplication of two functions in the k-space domain is equivalent to the convolution of the inverse Fourier transforms of the functions in the image domain.

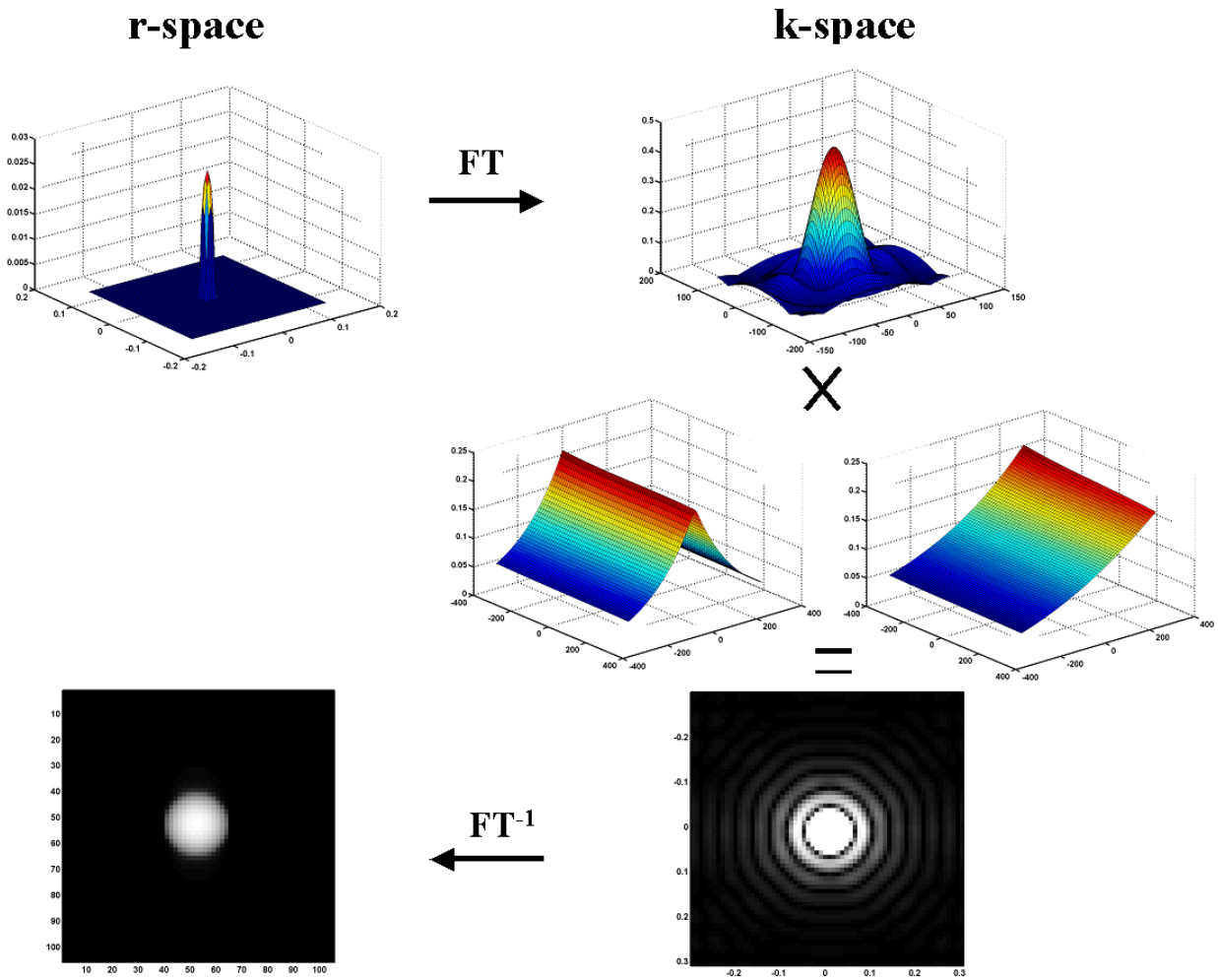

Figure 5.5: Schematic representation of the model used to obtain the effect of diffusion, relaxation and finite flip-angle on the image. Top left: projection of a sphere onto the z-axis. Top right: Fourier transform of the sphere's projection–the jinc-function. Middle right: k-space weighting for centric (l) and sequential (r) encoding schemes. Bottom right: weighted projection of a sphere in k-space displayed in image mode. Bottom left: weighted projection of a sphere in r-space displayed in image mode.

5.4 Gradient Echo Imaging

5.4.1 Gradient Echo Pulse Sequence

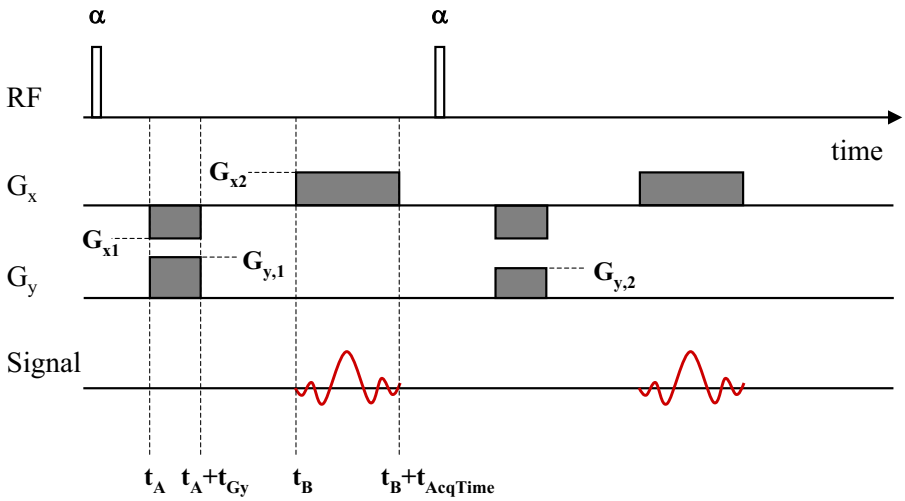

Figure 5.6: Pulse sequence used in gradient echo imaging. RF = excitation pulse, α = flip-angle, G_x = gradient waveform along x-direction, G_y = gradient waveform along y-direction, Signal = gradient echo.

Figure 5.6 shows a typical gradient echo pulse sequence. First, an RF pulse tips (or flips) the magnetization an angle α away from the z-axis. Then, imaging gradients G_x and G_y are applied. In general, when a gradient $\mathbf{G}$ is applied, spins at position $\mathbf{x}$ acquire a phase ϕ equal to

$$\begin{aligned} \phi(t) &= \gamma \int_0^t [\mathbf{G}(\tau) \cdot \mathbf{x}]\, d\tau = \gamma x \int_0^t G_x(\tau)\, d\tau + \gamma y \int_0^t G_y(\tau)\, d\tau \\ &= 2\pi k_x(t) x + 2\pi k_y(t) y, \end{aligned} \tag{5.20}$$

where in the last step we used Eq. 5.7. The above equation also tells us that the phase of the spins is proportional to the cumulative area $\int_0^t G(\tau) d\tau$ under a gradient waveform. Hence,

$$\phi(t) = \gamma x A(t)_{G_x} + \gamma y A(t)_{G_y}. \tag{5.21}$$

When the cumulative area under the gradient waveform–$A(t)_{G_x}$ or $A(t)_{G_y}$–is non-zero, the spins at different (x,y) locations accumulate a different amount of phase. The result is spin de-phasing. However, by detecting the amount of spin-incoherence at different spatial

locations, the spatial distribution (i.e, density) of spins can be mapped out. This is the image-domain perspective to position-encoding.[3] As the cumulative area under the gradient waveform reaches zero, the spins at different locations re-phase (i.e., $\phi(t)$ in Eq. 5.21 is zero for all values of x and/or y). The re-phasing of spins results in an echo. In other words, the coherence of spins, which has been lost during the application of position-encoding gradients, has been restored. Therefore, a gradient echo is produced whenever the cumulative area under the readout gradient G_x reaches zero. It is instructive to compare the occurrence of a gradient echo with the occurrence of a spin echo. In the spin echo case, the 180-degree pulses reverse the polarity of the gradients due to the static field inhomogeneities (i.e., *internal* gradients) halfway between the excitation and the middle of acquisition (time TE in Figure 4.11). The spin echo occurs when the cumulative area under these internal gradients reaches zero–exactly in the middle of the acquisition.

The basic principle behind the gradient and spin echoes is thus the same: gradient echoes as well as spin echoes occur when the cumulative area under a gradient waveform is zero (and therefore, $k = 0$). The difference is that in the case of spin echoes, it is the area under the *internal* gradient waveform, while in the case of gradient echoes, it is the area under the *external* gradient waveform that counts.

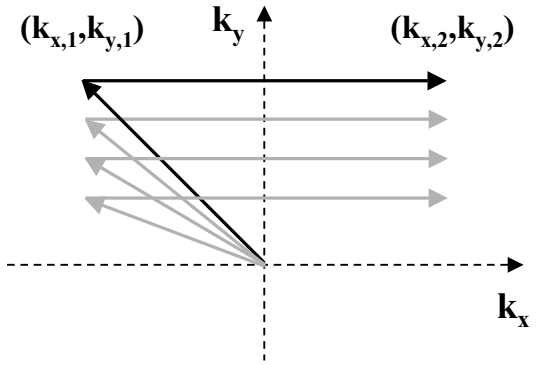

Figure 5.7: A schematic representation of k-space data collection in gradient echo sequence.

Figure 5.7 shows the k-space trajectory for the gradient echo sequence. Since each line of k-space is obtained with a "fresh" magnetization that has just been tipped away from the z-axis, we do not need to bring the k-vector back to zero (i.e., refocus the magnetization) after reading out a line of k-space.

[3]For the k-space perspective of position-encoding see Section 5.2.

5.4.2 *K*-Space Weighting for Gradient Echo Imaging

To construct k-space weighting for the gradient echo imaging sequence, we have to examine which processes contribute to signal decay along the readout and phase-encode directions, respectively. To study signal decay along the readout direction, we examine the k-space weighting in Eq. 5.19 (see also the pulse-sequence in Figure 5.6) at a fixed value of the phase-encode gradient (i.e., fixed y), or alternatively, after the nth excitation (at fixed n).

The nth excitation tips the magnetization an angle α away from the longitudinal axis. The projection of magnetization onto the transverse plane decays with with T_2^* relaxation constant. If the time between each excitation is TR, then the time up to the nth excitation is $t_1 = (n-1)TR$. Therefore, the k-space weighting after the nth excitation is

$$w(t) = \cos^{n-1}\alpha \ \sin\alpha \ \exp\left(-\frac{(n-1)TR}{T_1}\right) \ \exp\left(-\frac{t}{T_2^*}\right) \ \exp\left(-4\pi^2 D \int_0^t \left\{k_x^2(t') + k_y^2(t')\right\} dt\right). \tag{5.22}$$

Since we are concerned with signal decay during the acquisition period, the upper limit of the integration time t is $t_B < t < t_B + t_{AcqTime}$, where t_B is the time when the positive lobe of the readout gradient is turned on, while $t_B + t_{AcqTime}$ is the time when the positive lobe of the readout gradient is turned off (see Figure 5.6). If, in addition, we define the time when the phase-encode gradient lobe is turned on as t_A, and the time when it turned off as $t_A + t_{Gy}$, then we can solve the integrals in Eq. 5.22. For $t > t_B$,

$$\begin{aligned} w(t) \quad = \quad & \cos^{n-1}\alpha \ \sin\alpha \ \exp\left(-\frac{(n-1)TR}{T_1}\right) \ \exp\left(-\frac{t}{T_2^*}\right) \times \\ & \exp\left(-D\gamma^2\left\{-\frac{2}{3}\,t_{Gy}^3 G_{x1}^2 + t_{Gy}^2 G_{x1}^2 (t-t_A) - t_{Gy} G_{x1} G_{x2} (t-t_B)^2 + \frac{1}{3}\,G_{x2}^2 (t-t_B)^3\right\}\right) \times \\ & \exp\left(-D\gamma^2\left\{-\frac{2}{3}\,t_{Gy}^3 G_{y,n}^2 + t_{Gy}^2 G_{y,n}^2 (t-t_A)\right\}\right), \end{aligned} \tag{5.23}$$

where G_{x1} is the amplitude of the negative lobe of the x-gradient, G_{x2} is the amplitude of the positive lobe of the readout gradient and $G_{y,n}$ is the amplitude of the phase-encode gradient after the nth excitation. For a constant n, both, the diffusion term in Eq. 5.23 and the T_2^* relaxation depend on the time of the acquisition, t.[4] Signal decay along the readout direction will thus be caused by diffusion in the x and y-gradients and by the T_2^* relaxation.

To study signal decay along the phase-encode direction, we need to consider Eq. 5.22 for

[4]The cosine term and the T_1 relaxation term are constant for a given n value.

two consecutive excitations, for instance, the nth and *(n+1)*th. Doing so, we can see that the signal along k_y changes as a result of the additional projection onto the transverse axis ($\cos^{n-1}\alpha$ vs. $\cos^{n}\alpha$); as a result of additional T_1 decay ($e^{-(n-1)TR/T_1}$ vs. e^{-nTR/T_1}); and as a result of a different G_y amplitude ($G_{y,n}$ vs. $G_{y,n+1}$). As already mentioned before, the T_1 decay can be neglected for ^{3}He since the T_1 relaxation time for ^{3}He is on the order of hours, while the total imaging time is on the order of a minute. Therefore, it is a combination of the flip-angle effect and diffusion losses in the y-gradients that contribute to the changes along the phase-encode direction.

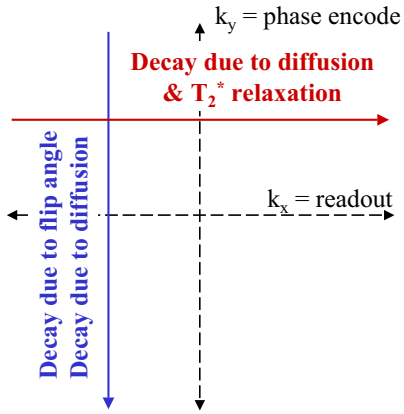

Figure 5.8: Schematic representation of signal decay during gradient echo sequence. Diffusion and T_2^* relaxation cause signal loss along the readout direction, while flip-angle and diffusion cause signal loss along the phase-encode direction.

Figure 5.8 summarizes, schematically, the processes which contribute to signal decay along the readout and phase-encode directions during gradient echo imaging of ^{3}He. As discussed above, diffusion and T_2^* relaxation affect the loss of signal along the readout direction (at constant n value), while diffusion and the size of the flip-angle affect the signal loss along the phase-encode direction.

5.4.3 2-D Gradient Echo Imaging Experiments and Simulations

Figures 5.9 and 5.10 demonstrate experimentally and theoretically the effect of diffusion, T_2^* relaxation and flip-angle on signal loss along the k_x and k_y directions, respectively. The magnitude of the raw k-space data is displayed on top of the page, followed by the simulation of the two-dimensional k-space and the k-space weighting which were obtained using the imaging parameters from the experiments.

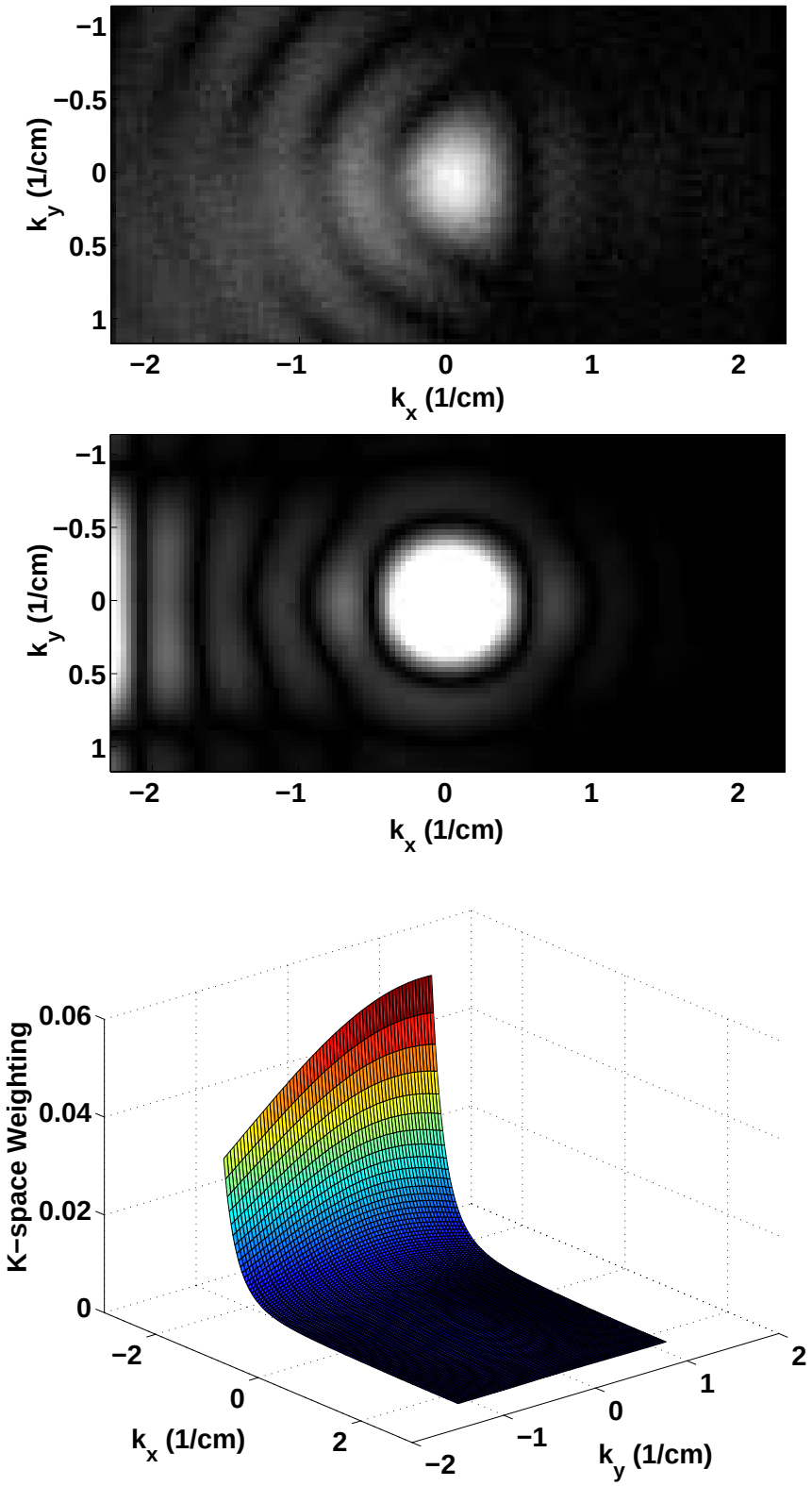

Figure 5.9: Diffusion and T_2^* losses along the readout direction. Top: Experimental raw k-space data. Middle: Simulation of k-space data. Bottom: K-space weighting used in the simulation. Acq.time=42.6 ms, BW=1502 Hz, $\alpha = 8°$, $FOV_x = FOV_y = 27.8$ cm, $\Delta x = 2.17$ mm, $\Delta y = 4.34$ mm, $T_2^* = 40$ ms, sequentially ordered phase-encode gradients.

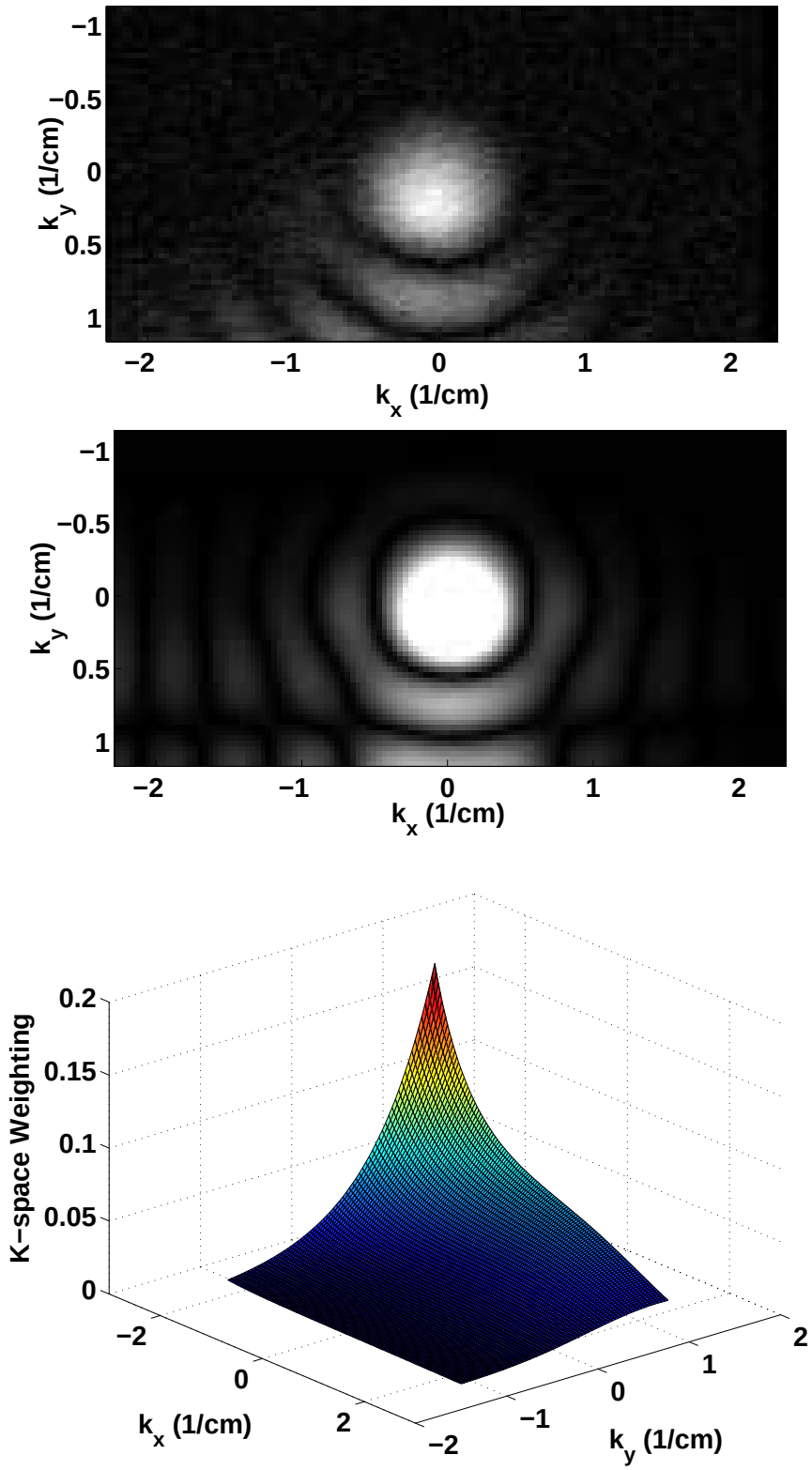

Figure 5.10: Flip-angle effects along the phase-encode direction. Top: Experimental raw k-space data. Middle: Simulation of k-space data. Bottom: K-space weighting used in the simulation. Acq.time=10.8 ms, BW=5952 Hz, $\alpha = 19.6°$, $FOV_x = FOV_y = 27.8$ cm, $\Delta x = 2.17$ mm, $\Delta y = 4.34$ mm, $T_2^* = 40$ ms, sequentially ordered phase-encode gradients.

To understand the appearance of partial concentric circles in the k-space data of Figures 5.9 and 5.10, we recall that the Fourier transform of a circle is a *jinc* function (see Figure 5.5) which is characterized by concentric circles spreading from the center ($k_x = 0,\ k_y = 0$) of k-space. In Figure 5.9, the intensity of concentric circles decreases from negative to positive k_x, which corresponds to the forward passage of time (see Eq. 5.10 as well as Figure 5.6). Such decay in signal intensity is indicative of excessive T_2^* relaxation and diffusion losses in the G_x gradient during the acquisition period. This can also be observed from the k-space weighting, which shows a large drop of relative NMR signal along the k_x direction. Ideally, we would like to minimize such asymmetric signal loss.

Similarly, the intensity of concentric circles in Figure 5.10 decreases from positive to negative k_y values (i.e., from the first to the last line of k-space scanned). However, in this case the loss of signal intensity must be attributed to flip-angle effects. In particular, if the flip-angle is too large, the magnetization could decay completely before the entire k-space plane is scanned. The flip-angle used to obtain the k-space data in Figure 5.10 was 19°, which turns out to be too large to utilize all the available magnetization in our gradient echo sequence the best way possible.[5] To see this, consider Eq. 5.13 for 64 phase-encoding steps ($n = 64$). To best utilize the available magnetization, we must *maximize* the SNR at the center of k-space while at the same time making sure not to run out of the magnetization before the end of the scan. The first condition is satisfied by looking for a maximum of the normalized signal $s(t, n, \alpha)/s_\circ(t)$ in Eq. 5.13 at $y = 0$, which corresponds to $n = 32$:

$$\begin{aligned} \frac{d\left[s(t, n = 32, \alpha)/s_\circ(t)\right]}{d\alpha} &= 0 = -31\cos^{30}\alpha\ \sin^2\alpha + \cos^{32}\alpha \\ \tan\alpha &= \sqrt{\frac{1}{31}} \\ \alpha &= 10.2^\circ. \end{aligned} \tag{5.24}$$

To satisfy the second condition we demand that we use 99% of gas polarization during the scan. Thus,

$$\begin{aligned} \frac{s(t, n = 64, \alpha)}{s_\circ(t)} &= \frac{s_\circ(t)\ \cos^{63}\alpha\ \sin\alpha}{s_\circ(t)} \approx 0.01 \\ \cos^{63}\alpha\ \sin\alpha &\approx 0.01 \\ \alpha &\approx 18.9^\circ. \end{aligned} \tag{5.25}$$

[5] Flip-angle calibration was done prior to imaging experiments by collecting FID data on a water sample (see also Section 4.6.1).

Therefore, for 64 phase-encoding steps, flip-angles around 15° offer a compromise between the need for maximum SNR in the middle of k-space and the need for optimal usage of the available magnetization. The calculations would need to be adjusted when using a different number of phase-encoding steps or a different encoding scheme.[6]

5.4.3.1 Centrally and Sequentially Ordered Phase-Encode Gradients during Gradient Echo Imaging

While the flip-angle can be optimized to provide uniform magnetization levels throughout the gradient echo imaging sequence [93], the diffusion losses (such as those in Figure 5.9) are, in principle, unavoidable. However, they can be minimized significantly by collecting low k-values prior to high k-values. Recall, that the diffusion loss is proportional to the cumulative path integral in k-space (see Eq. 5.17):

$$\ln \frac{s(t)}{s_\circ} = -4\pi^2 D \int_0^t \mathbf{k}^2(t')dt'. \tag{5.26}$$

Consequently, to reduce diffusion losses as much as possible, we would ultimately have to design a pulse sequence with a trajectory that starts at the origin of k-space and then spirals (or progresses) to the outer edges of k-space, such as the trajectories shown in Figure 5.11. However, we start by simply reorienting the phase-encode gradients in our gradient echo sequence. Instead of starting the scan of k-space at high k_y values where diffusion losses are large (Figure 5.12, right), we can start with the $k_y = 0$ line and then proceed with alternate scans on either side of the k-plane (Figure 5.12, left). This adjustment in the ordering of the phase-encode gradients is easy to implement into the pulse-sequence and does not require an elaborate algorithm during the image processing stage.

Figures 5.13 and 5.14 show, respectively, an image and a simulation of ^{3}He obtained using the gradient echo sequence with sequentially ordered phase-encode gradients (as displayed on the right side of the Figure 5.12). The x and y axes are the imaging axes in units of cm. The 2-D image of the sphere occupies a circular area with a diameter of about 2 cm, which is consistent with the size of the cell imaged ($r = 1.25$ cm). The vertical axis in both plots represents the intensity of the MR signal in arbitrary units.[7] The spike at the origin of

[6] For 128 phase-encoding steps, the ideal angle would be between 7.2° and 12.6°.

[7] The vertical scales of the image and simulation were not scaled against each other because the units used in the simulation represent the fraction of signal decay from the onset of imaging (i.e., when the

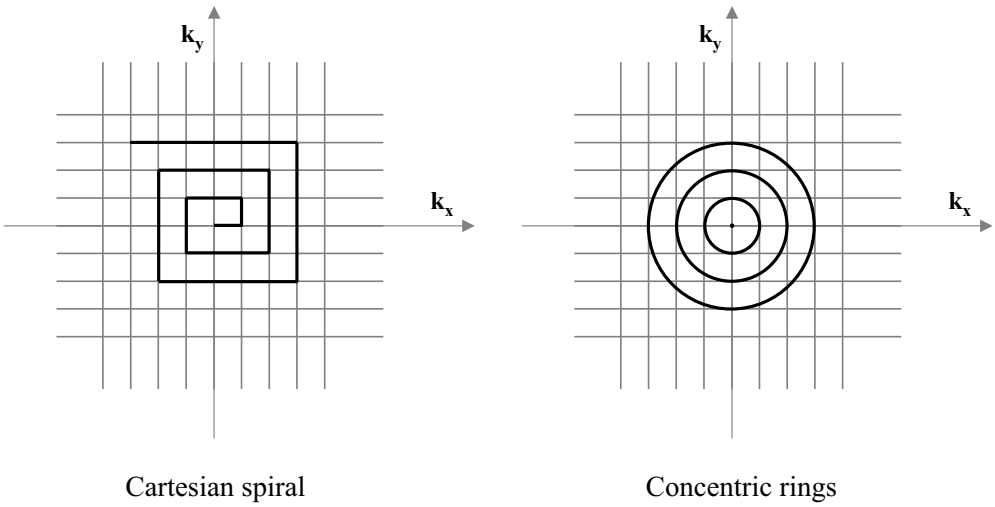

Figure 5.11: A schematic representation of k-space trajectories using a Cartesian spiral (left) and concentric circles (right) encoding scheme that can significantly reduce diffusion losses during imaging.

k-space is a DC signal, which results from a DC offset in any of the electronics components. It can be removed during signal processing.

Similarly, Figures 5.15 and 5.16 show, respectively, an image and a simulation of ^{3}He obtained using the gradient echo sequence with centrally ordered phase-encode gradients (as displayed on the left side of Figure 5.12). Both (central and sequential) gradient echo images were collected after 2 hours of optical pumping and using the same imaging parameters: the transmit-receive frequency of 397 kHz, a flip-angle of 15.5 degrees, resolution of 1.64 mm in x and y dimensions, field-of-view of 10.5 cm, acquisition time of 4 ms, receiver bandwidth of 8 kHz, G_x gradient equal to 4.7 mT/m and maximum G_y gradient value equal to 9.41 mT/m.

By comparing Figures 5.13 and 5.14 with Figures 5.15 and 5.16, we can determine the SNR gain in using centrally as opposed to sequentially ordered phase-encode gradients. To compare the SNR's in the actual data, we first notice that the noise levels in Figures 5.13 and 5.15 are approximately the same, with the average noise around 0.5 units. This is consistent with the fact that the same receiver bandwidth was used for both experiments.[8]

magnetization of the hyperpolarized gas was equal to 1), while the vertical scale in the experimental plots reflects the amount of voltage induced in the receiver coil during the scan. It would not be straightforward to normalize the detected voltage against the maximum voltage, in part due to the DC signal at the origin of k-space.

[8] As discussed in Section 3.2.2 on MRI noise properties, the amount of noise is proportional to the receiver bandwidth.

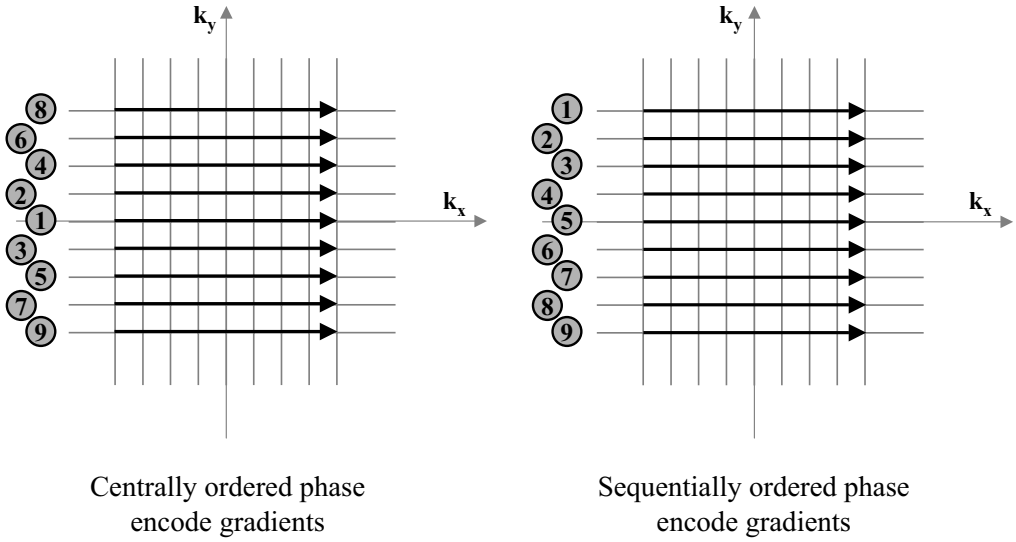

Figure 5.12: A schematic representation of centrally (left) and sequentially (right) ordered phase-encoding scheme using 2DFT sampling of k-space. By acquiring central phase-encodes first, diffusion losses are reduced.

To compare the signal levels, we would need to take the ratios of the volumes under the signal intensity function. However, to first order, we can approximate the ratio of the volumes with the ratios of the maximum signal intensity (ignoring the DC peak) because the projections onto the xy-plane are approximately the same for the two plots. Therefore, we have

$$\begin{aligned} \textit{SNR for sequentially ordered phase} - \textit{encode gradients} &\approx 17.4:1; \\ \textit{SNR for centrally ordered phase} - \textit{encode gradients} &\approx 4.4:1, \end{aligned}$$

and the SNR gain for gradient echo images obtained with centrally ordered phase-encode gradient is thus around 4.

Since the simulations do not model noise during the acquisition, we cannot estimate the SNR of the simulations. However, as demonstrated by the experimental data, the ordering of phase-encode gradients does not effect the noise level, which only depends on the receiver bandwidth. It thus suffices to compare the signal levels of the two simulations (Figure 5.13 and 5.16). The gain when using centrally ordered phase-encode gradient is approximately 3.

We can conclude that the actual data and simulation do agree to first order. The slight difference between experiment and simulation in the amount of signal gained using centrally

ordered phase-encode gradient could be attributed to various factors. First, the simulation assumes that the levels of magnetization at the onset of imaging are the same for the two experiments (centric and sequential encoding schemes). However, even though we attempted to pump the ^{3}He cell the same amount of time in both experiments, and in addition, to take the same amount of time from the end of the pumping process to the start of imaging, the levels of polarization might have been slightly different in the two experiments (due, for instance, to differences in pumping temperature, the cell-cooling process, changes in the gradient shim values). One way to avoid this uncertainty in the future would be to collect an FID signal before imaging, using a small flip-angle to minimize magnetization loss. This FID signal would serve as a marker (or detector) of the polarization levels at the onset of imaging.

Another possible cause of the SNR gain difference could be the uncertainty in the flip-angle used in the experiment. Since uncertainty in the flip-angle is cumulative with the number of excitations (due to the factor $\cos^{n-1}\alpha$ in Eq. 5.12), it will have a disproportionably larger effect on the experiment with sequentially rather than centrally ordered phase-encode gradients since the center of k-space occurs at $n = 33$. For instance, a 16% error in the flip-angle ($15.5^\circ \pm 2.5^\circ$) would produce a 22% error in the maximum signal intensity at $k = 0$ for sequentially ordered phase-encode gradients, and consequently, the signal gain in the simulation would become 3.11 ± 0.9, which would account for the entire difference between simulation and experiment.

Finally, in future experiments, a crusher gradient could be added into the pulse sequence after the acquisition period to destroy the remaining transverse magnetization before "fresh" magnetization is tipped from the longitudinal axis [68]. This is necessary whenever $TR < T_2^*$–a condition that indicates that T_2^* relaxation processes have not destroyed the transverse magnetization by the end of the TR period. In the experiments of Figure 5.17, $TR \approx 110$ ms, while $T_2^* = 30 - 60$ ms, so the gas magnetization should have decayed significantly by the end of the TR period.

Figure 5.17 shows our best gradient echo image (left) and projection onto y-axis (right) of hyperpolarized ^{3}He taken with centrally ordered phase-encode gradients after 10 hours of optical pumping. It is instructive to compare the SNR of the gradient echo image of a cell filled with hyperpolarized ^{3}He with the SNR of the gradient echo image of the same-sized cell filled with water. Figure 5.18 shows a water gradient echo image (left) and projection (right)

obtained with sequentially ordered phase-encode gradients.[9] Both hyperpolarized ^{3}He and water gradient images were collected at 398 kHz.

From the projections onto the y-axis, displayed on the right of Figures 5.17 and 5.18, we can see that the SNR of hyperpolarized ^{3}He is approximately 13, while the SNR for prepolarized water is 4. Hyperpolarized ^{3}He has thus a factor of approximately 3 higher SNR than prepolarized water when using a gradient echo sequence, 10 hours of optical pumping, and $B_p \approx 0.3$ T.

In conclusion, the gradient echo imaging of hyperpolarized gases is very straightforward to implement on the low-field pulsed resistive scanner once the flip-angle and the gradient waveform are chosen to provide a symmetric signal decay around the center of k-space. However, gradient echo imaging is an inefficient way of using the gas hyperpolarization due to the small flip-angles used for each excitation. We will examine spin echo imaging in the next chapter.

[9]Since water was pre-polarized before each 90-degree excitation, there was no detectable difference in the SNRs of the gradient echo image using centrally versus sequentially ordered phase-encode gradients.

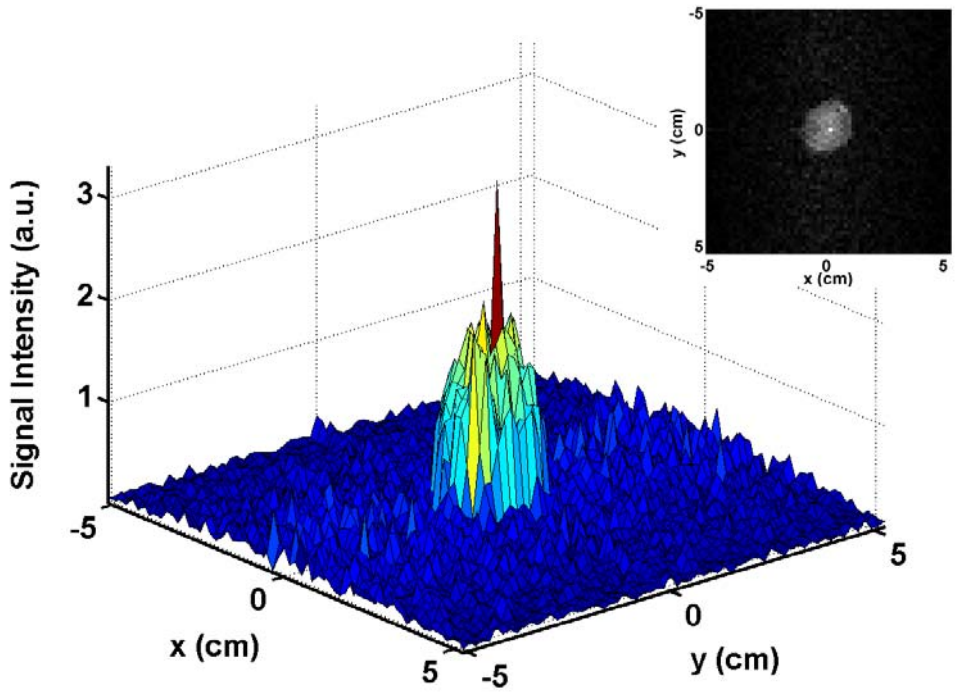

Figure 5.13: Gradient echo image of a 2.5 cm sphere filed with hyperpolarized ^{3}He obtained with **sequentially ordered** phase-encode gradients. Acq.time=4 ms, BW=8 kHz, $\alpha = 12.7°$, $FOV_x = FOV_y = 10.5$ cm, $\Delta x = \Delta y = 1.64$ mm, $t_{pump} = 2$ h, T_2^* relaxation negligible.

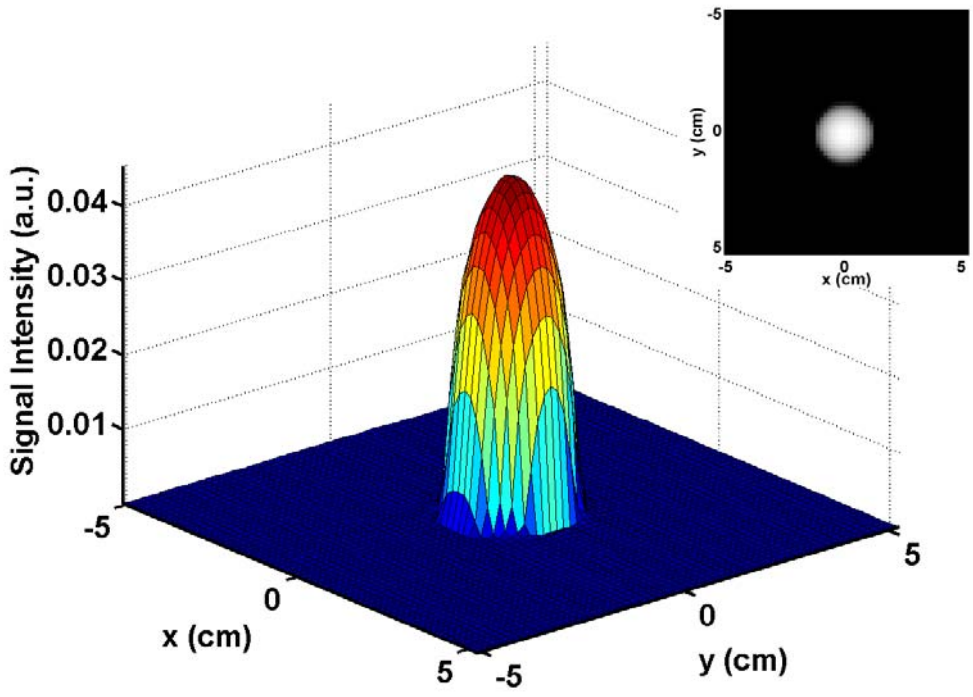

Figure 5.14: Simulation of the experiment displayed in the Figure 5.13.

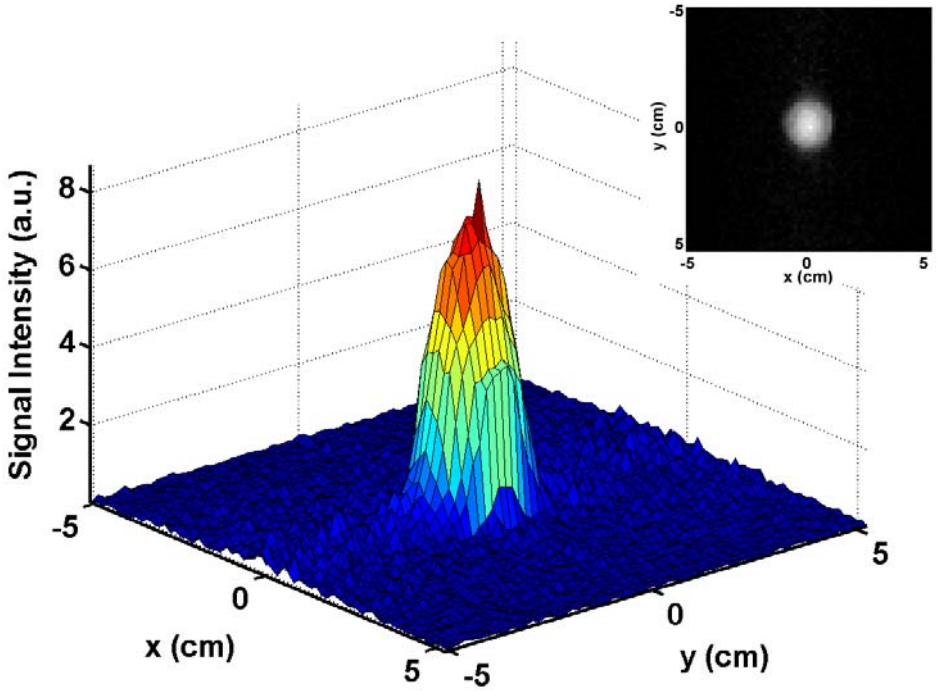

Figure 5.15: Gradient echo image of a 2.5 cm sphere filed with hyperpolarized ^{3}He obtained with **centrally ordered** phase-encode gradients. Acq.time=4 ms, BW=8 kHz, $\alpha = 12.7°$, $FOV_x = FOV_y = 10.5$ cm, $\Delta x = \Delta y = 1.64$ mm, $t_{pump} = 2$ h, T_2^* relaxation negligible.

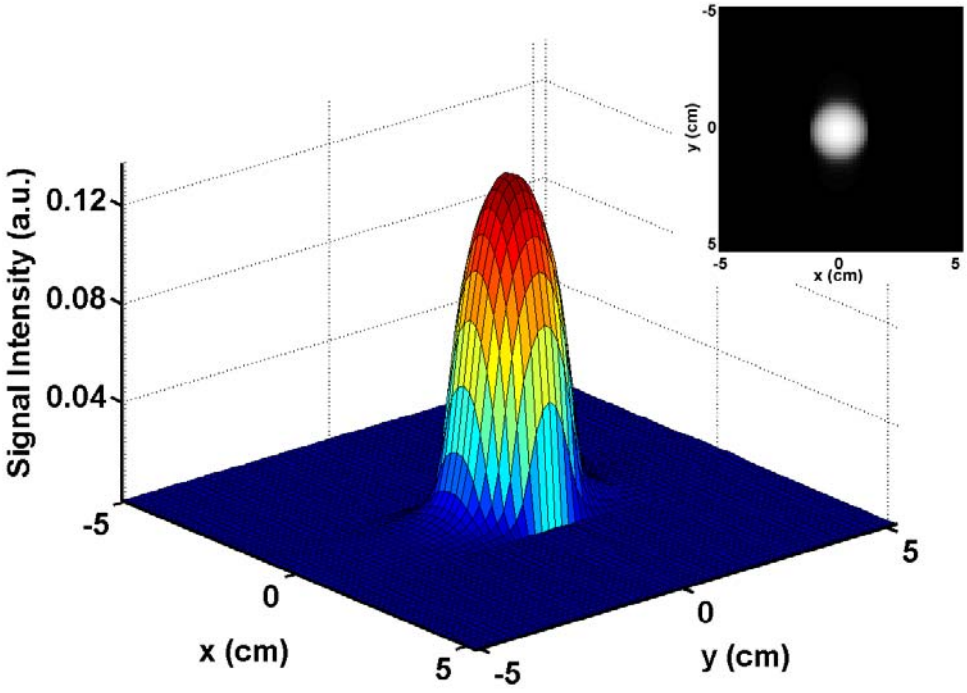

Figure 5.16: Simulation of the experiment displayed in the Figure 5.15.

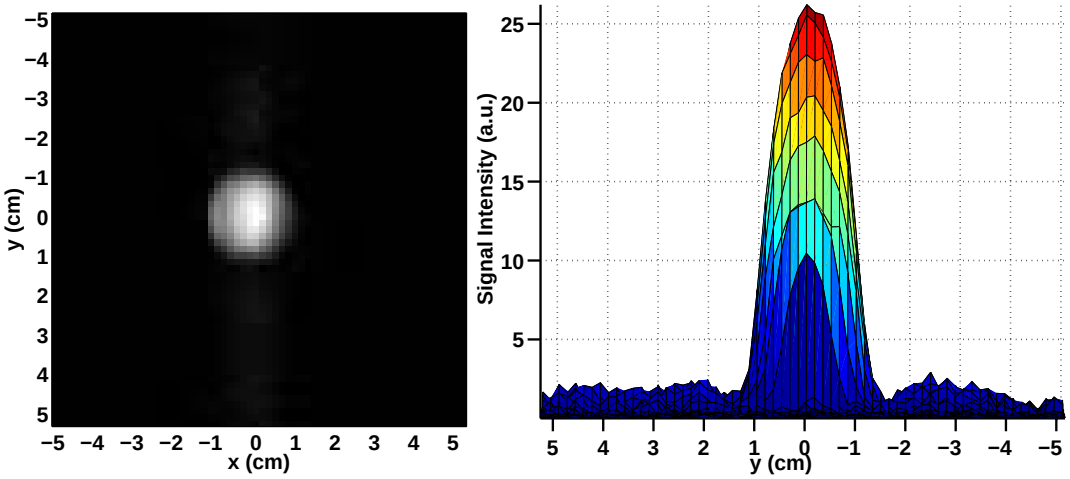

Figure 5.17: Gradient echo image (left) and projection (right) onto the y-axis of a 2.5 cm sphere filed with **hyperpolarized ^{3}He** using centrally ordered phase-encode gradients. $t_{OP} = 10$ h; $f_{RF} = 398$ kHz; $\alpha = 13°$; $\Delta x = \Delta y = 1.64$ mm; $FOV_x = FOV_y = 10.5$ cm; $T_{AcqTime} = 4$ ms; $BW = 8$ kHz; $G_x = 4.7$ mT/m; $G_y^{max} = 9.41$ mT/m.

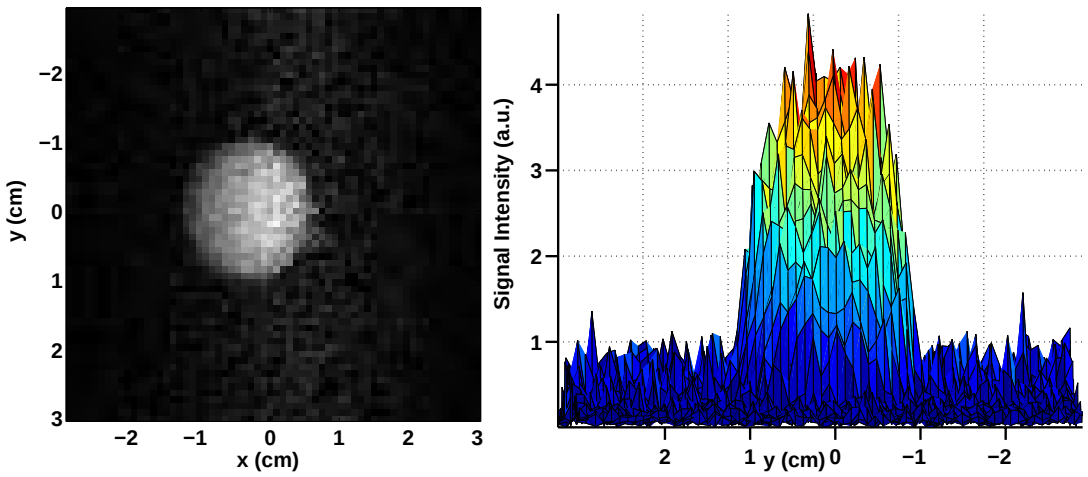

Figure 5.18: Gradient echo image (left) and projection (right) onto the y-axis of a 2.5 cm sphere filed with **doped water**. $B_p \approx 0.3$ T; $f_{RF} = 398$ kHz; $\alpha = 90°$; $\Delta x = \Delta y = 0.94$ mm; $FOV_x = FOV_y = 6$ cm; $T_{AcqTime} = 4$ ms; $BW = 8$ kHz; $G_x = 6.26$ mT/m; $G_y^{max} = 12.5$ mT/m.

5.5 Spin Echo Imaging

5.5.1 Spin Echo Pulse Sequence

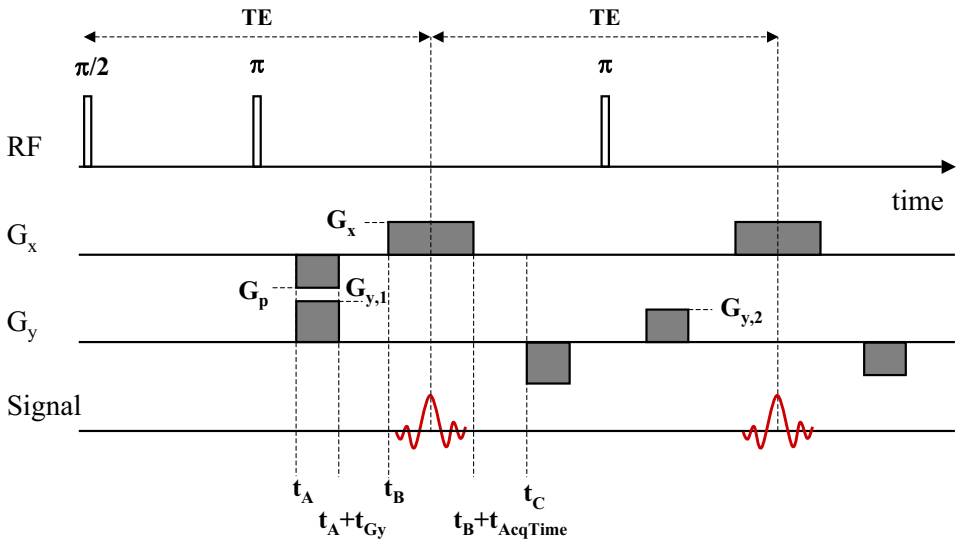

Figure 5.19: Pulse sequence used in spin echo imaging.

The spin echo imaging sequence is shown in Figure 5.19, while the k-space trajectory corresponding to this sequence in shown in Figure 5.20. The sequence is an extension of the CPMG sequence (see Figure 4.11 in Chapter 4.6) with the imaging gradients applied along the x and y direction. The spin echo occurs in the middle of the acquisition time, $t_{Acq\,Time}$, provided that the area under the negative x-gradient lobe is half the area under the positive x-gradient lobe. Unlike in the case of the gradient echo sequence, the phase-encode gradients are refocused after each acquisition to avoid error accumulation due to imperfect 180-degree pulses. An imperfect 180-degree pulse would flip only a fraction of the area under the y-gradient pulse, and consequently, the point $(k_{x,2}, k_{y,2})$ in Figure 5.20 would not map into its mirror image across the y-axis as it should. As a result, the k-space would be encoded improperly. The problem of imperfect 180-degree pulses could be avoided entirely if the k-space vector was at the origin of k-space before applying each 180-degree pulse. However, if the readout gradient was refocused in addition to the phase-encode gradients, diffusion losses might be too large. In this work, we focus exclusively on 1-D projection experiments using phase-encode gradients. The issues related to 2-D spin echo acquisition are briefly outlined in the conclusion of this chapter.

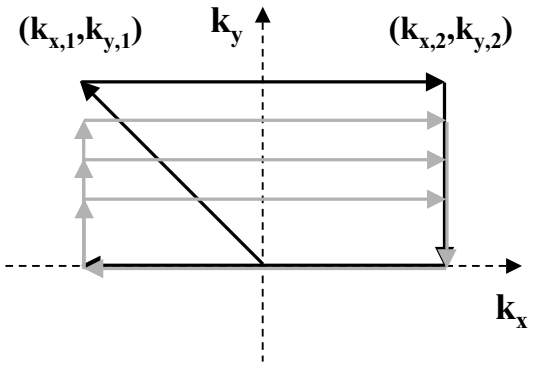

Figure 5.20: A schematic representation of k-space data collection in spin echo sequence.

5.5.2 *K*-Space Weighting for Spin Echo Imaging

The k-space weighting for spin echo imaging can be constructed following arguments similar to the ones used when designing the k-space weighting for gradient echo imaging. Unlike in the case of gradient echo imaging, however, the initial flip-angle in the spin echo imaging is 90°, which brings all the magnetization into the transverse plane. The 180-degree pulses are then used to refocus the magnetization every TE time period. Furthermore, since the magnetization is in the transverse plane during imaging, it decays exclusively due to the transverse T_2^{CPMG} relaxation. Finally, we also need to consider diffusion losses in the imaging gradients. The k-space weighting for spin echo imaging will thus be equal to

$$\begin{aligned} w(t) &= \left(\cos^{n-1} 90\right)(\sin 90)\exp\left(-\frac{t}{T_2^{CPMG}}\right)\exp\left(-4\pi^2 D\int_0^t \{k_x^2(t') + k_y^2(t')\}dt\right) \\ &= \exp\left(-\frac{t}{T_2^{CPMG}}\right)\exp\left(-4\pi^2 D\int_0^t \{k_x^2(t') + k_y^2(t')\}dt\right). \end{aligned} \tag{5.27}$$

In the above equation, the time integral must span the entire history of the magnetization vector which is being imaged. Since spin echo imaging is performed by continuously refocusing the same magnetization vector, t should be the time from the 90-degree excitation–when the magnetization was tipped into the transverse plane. Contrast this with gradient echo imaging, where t was the time elapsed from the last RF excitation.

We can divide the decay expressed in Eq. 5.27 into the decay along the readout (i.e., x) axis and the decay along the phase-encode (i.e., y) axis. If we ignore the T_2^{CPMG} relaxation

for a moment, then the decay along the readout and the phase-encode directions is entirely due to diffusion in the imaging gradients, as depicted in Figure 5.21. To find the diffusion term in Eq. 5.27 we need to express the x and y-gradients as a function of time and then integrate the gradients from the beginning of the imaging sequence to the time of interest. This procedure was performed numerically, using Matlab, as it has no simple close-form solution. Once the diffusion losses were modelled, the T_2^{CPMG} relaxation was added into the model in the form of a simple exponential decay whose time constant T_2^{CPMG} was based on the results obtained in Section 4.6. Figure 5.21 shows schematically, that the main process

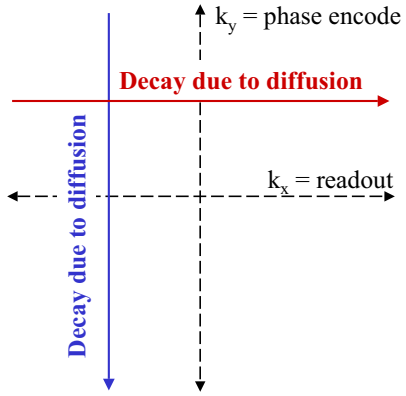

Figure 5.21: Schematic representation of signal decay during spin echo sequence. The main mechanism of signal loss in both readout and phase-encode directions is diffusion.

contributing to signal loss along the readout and phase-encode axis is diffusion.

5.5.3 1-D Spin Echo Imaging Experiments and Simulations

Since spin echo sequences are limited by large diffusion losses in the case of hyperpolarized gases, we examine a 1-D spin echo pulse sequence, with imaging gradients applied along the y-axis only (Figure 5.19 without the G_x gradient).

5.5.3.1 Centrally and Sequentially Ordered Phase-Encode Gradients

Gradient echo imaging of ^{3}He showed that using centrally rather than sequentially ordered phase-encode gradients improved the SNR of the image by a factor of 4. It is thus reasonable to investigate the SNR gain when using centrally ordered phase-encode gradients in the spin echo imaging sequence. To study this SNR improvement, we used the Pulsed Gradient Spin

Echo sequence (PGSE) introduced in Chapter 4.7 (see Figure 4.16). If the diffusion inducing gradients are advanced according to the centric/sequential ordering schemes (Figure 5.12), they mimic the centric/sequential ordering of phase-encode gradients in the 1-D spin echo sequence. However, since the echo was acquired at $k = 0$, the frequency distribution of the object had no bearing on the size of the spin echo which was thus purely a consequence of diffusion losses accrued during $t = \Delta$. In other words, by using the PGSE sequence rather than the 1-D spin echo sequence, we were able to assess directly the k-space weighting function for pulsed bipolar gradients (Chapter 5.3.4). Figure 5.22 shows the PGSE sequence with pulsed gradients advancing in either centric or sequential order.

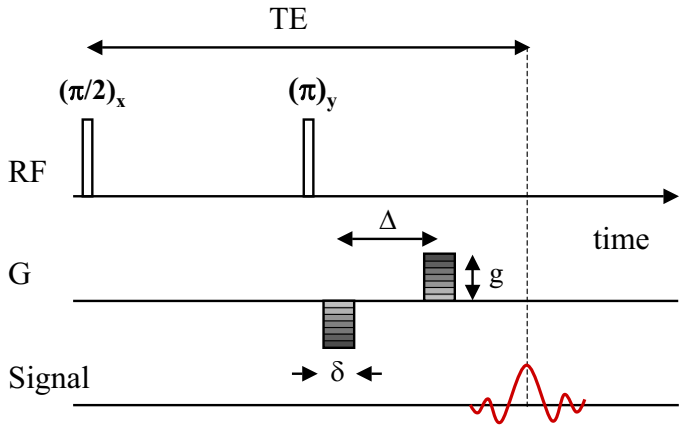

Figure 5.22: Pulsed gradient spin echo sequence.

Diffusion losses due to pulsed bipolar gradients were expressed in Chapter 4.7, Eq. 4.73. After accounting for T_2^{CPMG} relaxation losses, the k-space weighting for the nth echo is

$$w(nTE) = \exp\left[-D\, n\gamma^2 g^2 \delta^2 \left(\Delta - \frac{\delta}{3}\right) - \frac{nTE}{T_2^{CPMG}}\right]. \tag{5.28}$$

Since the gradient size g, duration δ, and separation Δ are known, while the T_2^{CPMG} relaxation time constant can be predicted from the measurements described in Section 4.8, we can directly calculate the relative magnitude of the nth echo and compare it to the experimental results.

Figure 5.23 shows experimental data and simulations of k-space weighting for ^{129}Xe as a function of k for both centrally and sequentially ordered bipolar gradients. The corre-

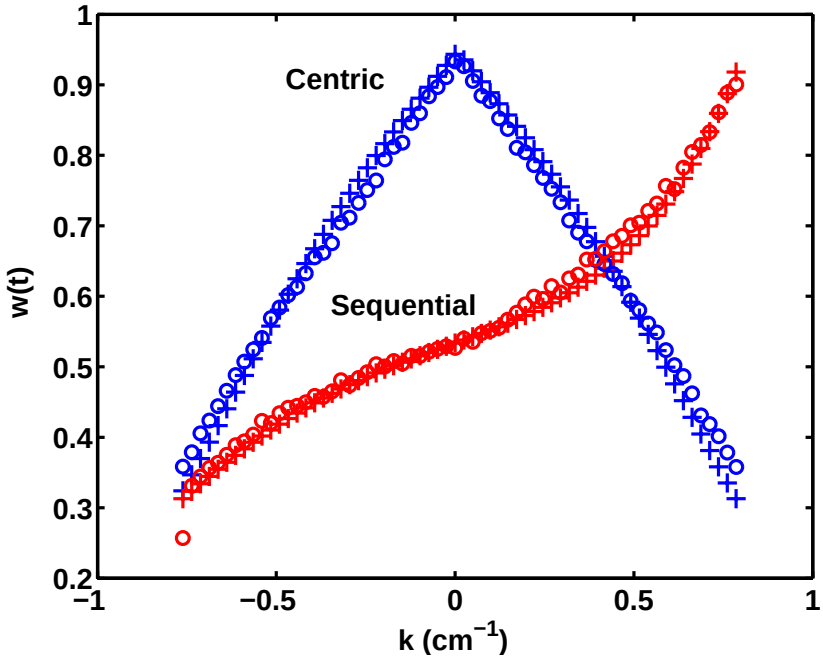

Figure 5.23: K-space weighting for ^{129}Xe using PGSE sequence with centric and sequential ordering - experimental data (circles), simulation (crosses). Predicts a $\times 2$ SNR gain using centric ordering. T_2 used in simulation = 6.5 s, g_{max} = 1.32 mT/m, Δg = 0.04 mT/m, δ = 5 ms, Δ = 10.36 ms, TE = 54.2 ms, Δy = 0.58 cm, FOV_y = 40.7 cm.

spondence between the simulation and the experimental data was best when ^{129}Xe T_2^{CPMG} relaxation time constant was chosen to be 6.5 s, which is reasonable in light of data displayed in Figure 4.22. The data obtained with the centric ordering scheme (Figure 5.12, left) peaks at $k = 0$, while the sequential ordering scheme (Figure 5.12, right) peaks at the positive edge of k-space, reflecting the fact that the first line of k-space is acquired with maximum available magnetization. Furthermore, since diffusion losses are proportional to the square of k, the k-space weighting function decays slower for centric than sequential ordering scheme. For an imaging resolution of 5.6 mm, there is a factor of two improvement in the intensity of the signal at the center of k-space when using centric ordering scheme. For a higher resolution, we expect an even faster decay of magnetization because stronger gradients have to be used to reach larger k-space values.

Figure 5.24 shows a simulation of the diffusion k-space weighting for ^{129}Xe at a higher imaging resolution (2 mm). As predicted, the difference in signal intensity in the center of k-space when using centrally versus sequentially ordered bipolar pulsed gradients is very pronounced. This effect is even bigger for ^{3}He, because it has a larger diffusion constant

than ^{129}Xe. Figure 5.25 shows diffusion k-space weighting for ^{3}He, for a resolution of 5 mm.

When k-space data is transformed into the image domain, the signal intensity at $k = 0$ determines the image SNR. Our experiments and simulations using PGSE pulse sequence have thus demonstrated that the SNR of the hyperpolarized gas images should improve significantly when using centrally ordered phase-encode gradients. We tested this assumption by performing 1-D imaging experiments with centric and sequential ordering schemes.

The 1-D imaging experiments were performed using only the G_y gradient in the spin echo imaging sequence, shown in Figure 5.19. Figure 5.26 shows a projection image of a sphere filled with hyperpolarized ^{3}He. Note that the image obtained with sequentially ordered phase-encode gradients has been multiplied by a factor of 50. The SNR gain in using centric ordering scheme is on the order of 100.

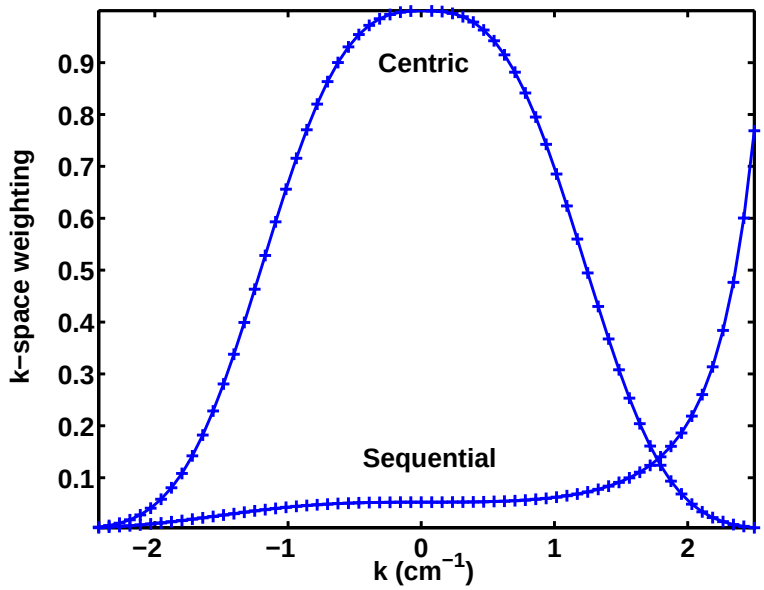

Figure 5.24: Diffusion k-space weighting–simulation for ^{129}Xe. Predicts a $\times$20 SNR increase for a 2 mm target resolution using centric encoding. No T_2^{CPMG} relaxation. $\Delta y = 2$ mm, $FOV_y = 12.8$ cm, $G_{max} = 4.2$ mT/m, $\Delta G = 0.13$ mT/m, $\delta = 5$ ms, $\Delta = 10$ ms, $TE = 20$ ms.

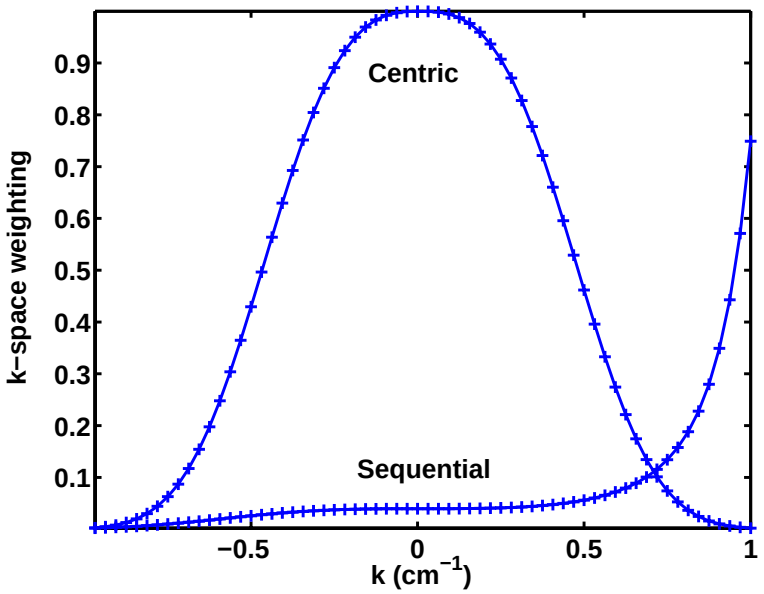

Figure 5.25: Diffusion k-space weighting–simulation for ^{3}He. Predicts a $\times$20 SNR increase for a 5 mm target resolution using centric encoding. No T_2^{CPMG} relaxation. $\Delta y = 5$ mm, $FOV_y = 32$ cm, $G_{max} = 1.54$ mT/m, $\Delta G = 0.05$ mT/m, $\delta = 2$ ms, $\Delta = 5$ ms, $TE = 10$ ms.

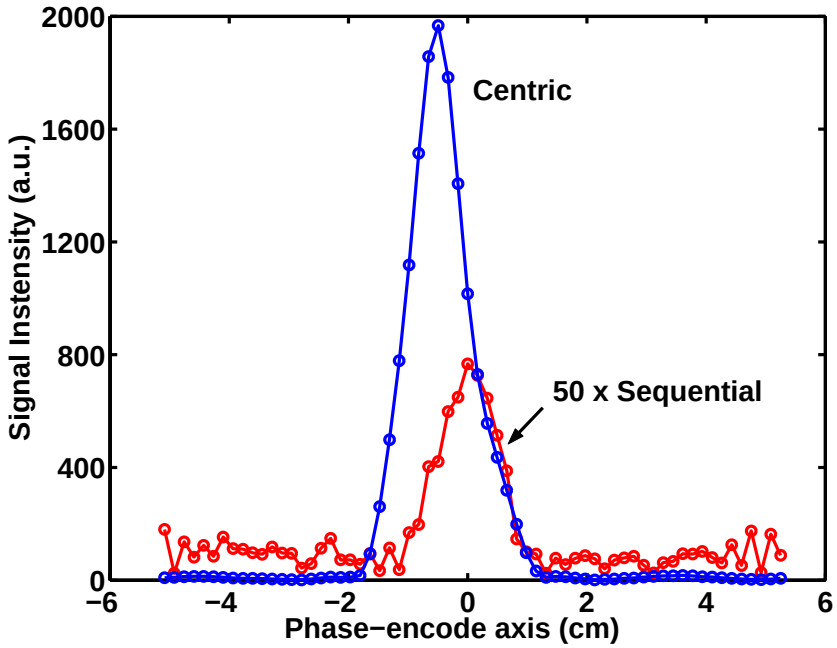

Figure 5.26: A 1-D spin echo image of a 2.5 cm sphere filled with hyperpolarized ^{3}He taken with centrally and sequentially ordered phase-encode gradients. Acquisition time = 4 ms, $FOV_y = 10.5$ cm, $\Delta y = 1.64$ mm, $G_{y,max} = 9.4$ mT/m, $\Delta G_y = 0.29$ mT/m.

5.6 Conclusions

The most commonly used sequences for imaging hyperpolarized gases are small flip-angle sequences, such as FLASH, which use a fraction of gas hyperpolarization to encode each line of k-space. These sequences are straightforward and easy to implement as they have very liberal phase requirements; however, they do not utilize all the available hyperpolarized gas magnetization.

In this work we modelled signal decay during gradient echo imaging which resulted from the flip-angle, relaxation and diffusion of the gas. We were able to determine the optimal flip-angle to avoid a non-uniform sampling of the phase-encode axis of k-space and show a factor of three improvement in the image SNR when using centrally ordered phase-encode gradients. Our gradient echo images using centric and sequential ordering scheme agreed with simulations to first order. Finally, comparing ^{3}He and water gradient echo images we find a factor of three improvement in the image SNR when using hyperpolarized ^{3}He.

Other researchers have studied in detail gradient echo imaging and the issues related to the flip-angle used. Zhao *et al.* [68] compared the quality of hyperpolarized ^{129}Xe images when using constant flip-angle (CFA) with sequential phase-encode gradients, CFA with centric phase-encode gradients, and a sequence with a variable flip-angle (VFA) which maintains a constant transverse magnetization throughout the duration of imaging. The researchers concluded that the VFA approach significantly improves the SNR of ^{129}Xe images and eliminates image artifacts which are unavoidable when using CFA with centric encoding scheme. Our images which were collected with centric ordering of phase-encode gradients and with constant flip-angle show no artifacts because of the nature of the object being imaged. A spherical object, such as our cell, contains almost no high frequency components in k-space domain.[10] Consequently, we were not affected by having a greatly depleted magnetization when collecting high frequency components in the case of centrally ordered phase-encode gradients. In the future, we would need to apply our model to a more realistic object–one that contains high frequency components. Since past research [68, 78, 95] shows an improved SNR when using variable flip-angles, it would be useful to implement the variable flip-angle algorithm on the pulsed resistive low-field scanner.

While the gradient echo sequences enabled us to obtain hyperpolarized gas images,

[10] This is because a sphere has no sharp edges, which would contribute high frequency components to the Fourier transform of a sphere.

the focus of our work was spin echo imaging. Single-shot CPMG spin echo sequences use all the available gas magnetization and thus offer greater SNR efficiency than small flip-angle sequences. At low magnetic field strengths at which we are operating, the gradient inhomogeneities and susceptibility effects are reduced, so the T_2 relaxation times of gases are long enough to allow for the collection of the entire k-space in a single-shot. The disadvantage is that spin echo sequences are limited by large diffusion losses in the case of hyperpolarized gases.

In this work we studied ways of minimizing diffusion losses. Since signal decay depends on the path integral over k-space, diffusion can be minimized by collecting low k-space values first. Our experimental spin echo data using a pulsed gradient spin echo sequence (PGSE) with centric and sequential ordering of phase-encode gradients agrees well with simulations and shows an improvement in the SNR when using centric ordering scheme. Finally, we collected 1-D projection spin echo images of ^{3}He. There was a factor of 100 improvement in the image SNR when using centric as opposed to sequential ordering of phase-encode gradients. However, large diffusion losses prevented us from obtaining 2DFT spin echo images.

Durand *et al.* [26, 89] used a RARE sequence for *in vivo* imaging of human lungs at low field (0.1 T). The diffusion coefficient of hyperpolarized gases in lungs is greatly reduced, because the alveolar structure of the lungs restricts gas diffusion. The apparent diffusion of ^{3}He, for instance, is around 2×10^{-5}, which is 10 times less than the unrestricted diffusion coefficient [26]. The smaller diffusion coefficient enabled the authors to obtain 2-D RARE images of human lungs. However, the authors were not able to obtain good quality cell images with the 2-D RARE sequence [26]. This fact indicates that spin echo imaging holds more promise for *in vivo* than *in vitro* imaging. The authors also concluded that the maximum resolution achievable with RARE (in the *in vivo* case) was 6 mm. However, this resolution might be surpassed, if a different phase-encoding scheme were used.

The ideal 2-D RARE sequence for low-field hyperpolarized gas imaging would be an outward sequence of rings, as described in [96] for other applications. The diffusion losses of this 2-D sequence would likely be dominated by crusher pulses, so RF-insensitive spin echo pulses [97] will be important to obviate crushers, and the increased SAR (specific absorption rate) would be well below safety limits for low-field MRI.